

# PROCEEDINGS OF SPIE

[SPIDigitalLibrary.org/conference-proceedings-of-spie](https://SPIDigitalLibrary.org/conference-proceedings-of-spie)

## A few novel phenomena in electromagnetic scattering

Yang, Yi, Soljačić, Marin

Yi Yang, Marin Soljačić, "A few novel phenomena in electromagnetic scattering," Proc. SPIE 11289, Photonic and Phononic Properties of Engineered Nanostructures X, 112891T (26 February 2020); doi: 10.1117/12.2554675

**SPIE.**

Event: SPIE OPTO, 2020, San Francisco, California, United States

# A few novel phenomena in electromagnetic scattering

Yi Yang and Marin Soljačić

Research Laboratory of Electronics, Massachusetts Institute of Technology, Cambridge,  
Massachusetts 02139, USA

## ABSTRACT

In this talk, we present some of our recent results in electromagnetic scattering, including a non-classical framework demonstrated via far-field scattering from nanophotonic structures, radiation sources via near-field scattering from free electrons, as well as synthetic scattering with non-Abelian gauge fields.

**Keywords:** Free-electron radiation, Bound states in the continuum, Quantum plasmonics, Nonlocality, Feibelman d parameters, Synthetic gauge fields, Non-Abelian, Aharonov–Bohm

## 1. INTRODUCTION

Scattering of electromagnetic waves is fundamentally related to the inhomogeneity of photonic systems. The inhomogeneity, i.e. the obstacle, can vary between microscopic to macroscopic scales; it can be an electron, a nanoantenna, or even a uniform slab. When an external electromagnetic excitation acts upon the obstacle, it creates secondary oscillation (besides the original incident waves) in the obstacle. The extra, secondary electromagnetic oscillation also re-radiates. These secondary oscillation and re-radiation are known as electromagnetic scattering. Aside from scattering, the secondary oscillation also transforms into thermal energy, which is known as absorption. Taken together, the summation of scattering and absorption are called extinction.

Perhaps the most famous electromagnetic scattering theory is the Mie theory that was developed over a hundred years ago. In the Mie theory, the obstacles are limited to spherical particles. Beyond the Mie theory, the development of electromagnetic computational techniques has enabled rigorous numerical solutions to various scattering problems, including both the nonretarded and retarded regimes. Moreover, thanks to nanotechnology and the flourish of plasmonics and topological photonics, there have been continuous advances in electromagnetic scattering over the past two decades.

In this talk, we will discuss several of our recent results on far-field, near-field, and synthetic scattering. First, we will present a general framework for nanoscale electromagnetism. The framework is featured by surface response functions known as Feibelman d-parameters, which allows a direct account of surface-related nanoscale, quantum corrections. We introduces the ‘ellipsometry’ for the surface response functions, enabled by the observation of large nonclassical spectral shifts and the breakdown of Kreibig broadening in far-field scattering measurements. Second, we will treat free-electron radiation as near-field scattering and derive a universal upper limit to their spontaneous emission and energy loss. Such an upper limit allows us to identify a slow-electron-efficient regime of radiation operation and methods for enhancing the emission probability. Finally, we will discuss a synthetic scattering phenomena featured by non-Abelian (non-commutative) gauge fields. Based on optical mode degeneracy, we break time-reversal symmetry in different manners to synthesize tunable non-Abelian gauge fields in real space. The interference of two final states, obtained by reversely-ordered path integrals, enables us to observe the non-Abelian Aharonov–Bohm effect with optical waves.

---

Further author information:

Y.Y.: E-mail: yiy@mit.edu

M.S.: E-mail: soljadic@mit.edu

## 2. FAR-FIELD SCATTERING: MEASUREMENT OF ELECTROMAGNETIC SURFACE RESPONSE FUNCTIONS

The macroscopic electromagnetic boundary conditions (BCs) have been well-established for over a century. They have proven extremely successful at macroscopic length scales, across all branches of photonics. Even state-of-the-art nanoplasmonic studies, exemplars of extremely interface-localized fields, rely on their validity. This classical description, however, neglects the intrinsic electronic length scale associated with interfaces. This omission leads to significant discrepancies between classical predictions and experimental observations in systems with deeply nanoscale feature-sizes, typically evident below  $\sim 10\text{--}20\text{ nm}$ .

We introduce and experimentally demonstrate a framework<sup>1</sup> that reintroduces the missing electronic length scales via surface response functions known as Feibelman  $d$ -parameters.<sup>2</sup> We establish an experimental procedure to ellipsometrically measure these complex, dispersive surface response functions, enabled by quasi-normal-mode theory and observations of pronounced nonclassical effects. Our results provide a general framework for modelling and understanding of any nanoscale (i.e. all relevant length scales  $\gtrsim 1\text{ nm}$ ) electromagnetic phenomena.

We reintroduce the electronic length scales by amending the classical boundary conditions with a set of mesoscopic complex surface response functions, known as the Feibelman  $d_{\perp}$ - and  $d_{\parallel}$ -parameters (Fig. 1a):<sup>2</sup> they play a role analogous to the local bulk permittivity, but for interfaces between two materials.  $d_{\perp}$  and  $d_{\parallel}$  are the missing electronic length scales—respectively equal to the frequency-dependent centroids of induced charge and normal derivative of tangential current at an equivalent planar interface (Fig. 1b). They enable a leading-order-accurate incorporation of nonlocality, spill-out, and surface-enabled Landau damping (tunnelling and size quantization, not incorporated in  $d$ -parameters, are non-negligible at feature-sizes below  $\approx 1\text{ nm}$ ).

The  $d$ -parameters drive an effective nonclassical *surface* polarization  $\mathbf{P}_s \equiv \boldsymbol{\pi} + i\omega^{-1}\mathbf{K}$  (Fig. 1b), with  $d_{\perp}$  contributing an out-of-plane surface dipole density  $\boldsymbol{\pi} \equiv d_{\perp}\varepsilon_0\llbracket E_{\perp} \rrbracket \hat{\mathbf{n}}$  and  $d_{\parallel}$  an in-plane surface current density  $\mathbf{K} \equiv i\omega d_{\parallel}\llbracket \mathbf{D}_{\parallel} \rrbracket$ . Here,  $\llbracket \mathbf{f} \rrbracket \equiv \mathbf{f}^+ - \mathbf{f}^-$  denotes the discontinuity of a field  $\mathbf{f}$  across an interface  $\partial\Omega$  with outward normal  $\hat{\mathbf{n}}$ ; similarly,  $f_{\perp} \equiv \hat{\mathbf{n}} \cdot \mathbf{f}$  and  $\mathbf{f}_{\parallel} \equiv (\hat{\mathbf{I}} - \hat{\mathbf{n}}\hat{\mathbf{n}}^T)\mathbf{f}$  denote the (scalar) perpendicular and (vectorial) parallel components of  $\mathbf{f}$  relative to  $\partial\Omega$ . These surface terms can be equivalently incorporated as a set of mesoscopic BCs for the conventional macroscopic Maxwell equations

$$\llbracket D_{\perp} \rrbracket = -i\omega^{-1}\boldsymbol{\nabla}_{\parallel} \cdot \mathbf{K} = d_{\parallel}\boldsymbol{\nabla}_{\parallel} \cdot \llbracket \mathbf{D}_{\parallel} \rrbracket, \quad (1a)$$

$$\llbracket B_{\perp} \rrbracket = 0, \quad (1b)$$

$$\llbracket \mathbf{E}_{\parallel} \rrbracket = -\varepsilon_0^{-1}\boldsymbol{\nabla}_{\parallel}\pi = -d_{\perp}\boldsymbol{\nabla}_{\parallel}\llbracket E_{\perp} \rrbracket, \quad (1c)$$

$$\llbracket \mathbf{H}_{\parallel} \rrbracket = \mathbf{K} \times \hat{\mathbf{n}} = i\omega d_{\parallel}\llbracket \mathbf{D}_{\parallel} \rrbracket \times \hat{\mathbf{n}}. \quad (1d)$$

It can be seen that these mesoscopic boundary conditions generalize the usual macroscopic electromagnetic BCs— $\llbracket D_{\perp} \rrbracket = \llbracket B_{\perp} \rrbracket = 0$  and  $\llbracket \mathbf{E}_{\parallel} \rrbracket = \llbracket \mathbf{H}_{\parallel} \rrbracket = \mathbf{0}$ —to which they reduce in the limit  $d_{\perp} = d_{\parallel} = 0$ .

We designed and fabricated film-coupled nanodisks (Figs. 1c) of various materials, to verify our framework and directly measure the  $d$ -parameters. Specifically, an optically-thick Au film (atop a Si substrate) is separated from lithographically defined Au, Al, and Si nanodisks (diameter,  $D$ ) by a nanoscale  $\text{AlO}_x$  spacer, deposited by atomic layer deposition, demarcating a film–nanodisk gap of thickness  $g$ . The fundamental dipolar gap plasmon resonance is optically accessible in the far field and exhibits highly confined electromagnetic fields within the gap, suggesting potentially large nonclassical corrections (Fig. 1d). In our experiment, we swept the disk diameter and gap size of Au nanodisks and measured their scattering spectra using dark-field scattering microscopy. The dipolar resonance is consistently blueshifted relative to the classical prediction, with shifts exceeding 30% for the smallest considered gaps (Fig. 1e). There are two reasons for such significant nonclassical shift. First, the nonclassical perturbation strength is much larger than in e.g. standalone nanospheres or film-coupled nanospheres, due to strong field-confinement beneath the entire nanodisk footprint. Second, screening from the  $\text{AlO}_x$  cladding expels induced charge into Au, thereby enhancing  $d_{\perp}^{\text{Au-AlO}_x}$  relative to the unscreened interface. Such large nonclassical spectral shifts enable us to extract the surface response functions based on quasi-normal-mode perturbation theory.

Figures 1fg show the measured dispersive, complex surface-response function  $d_{\perp}^{\text{Au-AlO}_x}(\omega)$ . Within the considered spectral range,  $\text{Re } d_{\perp}^{\text{Au-AlO}_x}$  (Fig. 1f) reveal a nearly dispersionless surface response of comparatively

large magnitude, from  $-0.5$  nm to  $-0.4$  nm. In contrast,  $\text{Im } d_{\perp}^{\text{Au-AlO}_x}$  (Fig. 1g) is strongly dispersive, increasing from  $\lesssim 0.1$  nm in the near-infrared to  $\approx 0.3$  nm in the visible. The measured dispersion (Fig. 1fg) only deals with a single plasmonic interface ( $\text{Au-AlO}_x$ ); it calls for the compilation of databases of  $d$ -parameters at interfaces of photonic and plasmonic prominence, analogous and complimentary to the existing databases of local bulk permittivities.

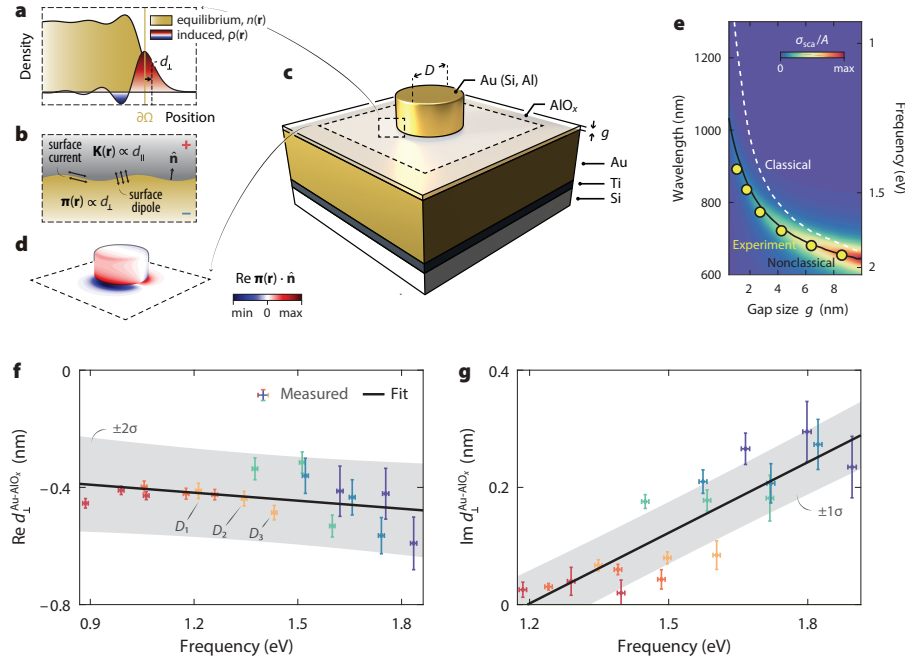


**Figure 1. Framework, experimental structure, measured nonclassical shifts, and surface response dispersion<sup>1</sup>** **a.** Equilibrium and induced densities.  $d_{\perp}$  is the centroid of induced charge. **b.** Nonclassical corrections can be formulated as self-consistent surface polarizations, representing effective surface dipole density  $\pi(\mathbf{r})$  and current density  $\mathbf{K}(\mathbf{r}) \propto d_{\perp}$ . **c.** Experimental structure. **d.** Nonclassical surface dipole density  $\pi(\mathbf{r})$  of the fundamental dipolar gap plasmon of a film-coupled Au nanodisk. **e.** Observation of large nonclassical corrections (spectral shift  $\gtrsim 400$  nm) in film-coupled Au nanodisks. Measured frequencies (circles) of the resonance blueshift relative to the classical prediction (dashed line) and quantitatively agree with nonclassical calculations. **f–g.** Measured (markers) dispersion of  $\text{Re } d_{\perp}^{\text{Au-AlO}_x}$  (**f**) and  $\text{Im } d_{\perp}^{\text{Au-AlO}_x}$  (**g**) and their linear fits (lines).

### 3. NEAR-FIELD SCATTERING: MAXIMAL SPONTANEOUS FREE-ELECTRON RADIATION

In the previous section, the background fields in the dark-field scattering measurement are plane waves from the far field. In this section, we will focus on the scattering problem of a near-field excitation, which are free electrons. We will discuss the electron energy loss and radiation in the spontaneous regime, where the velocity of electrons is assumed constant.

Free electrons interacting with an arbitrary optical environment or structure offer a versatile source of light, providing multiple pathways for spontaneous photon emission such as Cherenkov radiation, Smith–Purcell radiation, and transition radiation. The diversity of optical environments and applications yields widely varying radiation rates, within a multitude of theoretical approaches and experimental interpretations—this plethora of perspectives exposes a fundamental, yet unanswered question: How much radiation can ultimately be extracted from free electrons?

We theoretically derive and experimentally probe universal upper limits for the photon emission and energy loss of free electrons.<sup>3</sup> The limits, built upon passivity constraints, depend solely on the material composition and on the electron velocity and trajectory. We identify optimal electron velocities that vary with beam location;

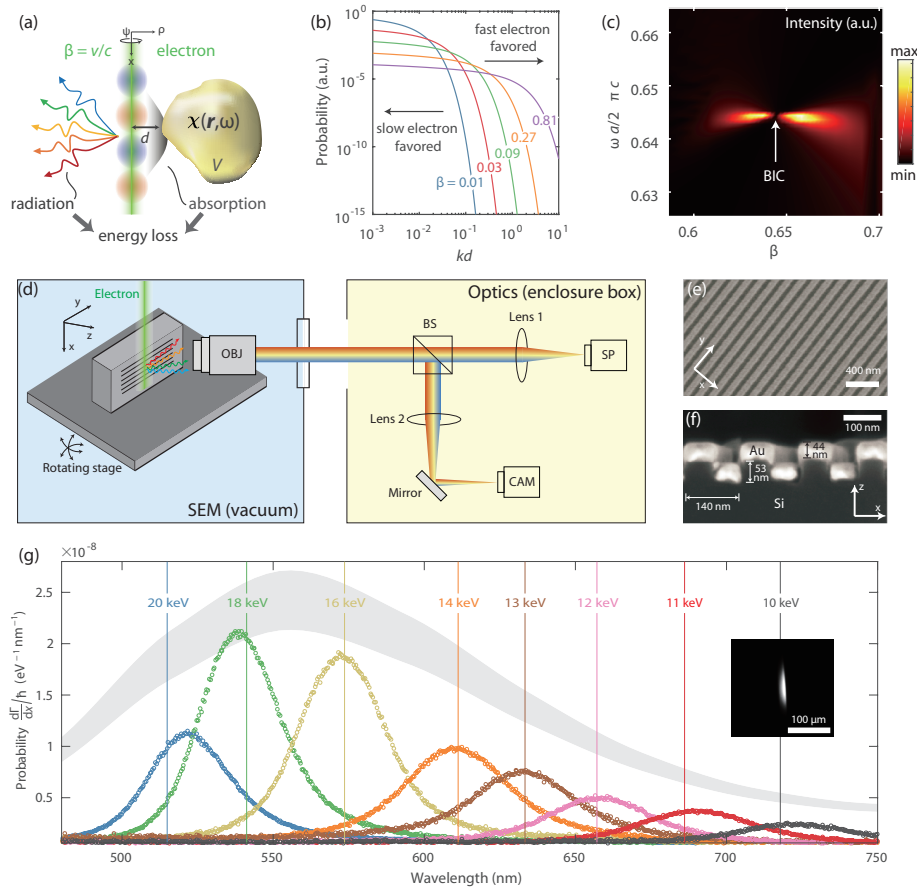


Figure 2. **Fundamental limit of free electron emission and its experimental test.**<sup>3</sup> (a) The interaction between a free electron and an obstacle defined by a susceptibility tensor  $\chi(\mathbf{r}, \omega)$  within a volume  $V$ , located at a distance  $d$ , generates electron energy loss into radiation and absorption. (b) Shape-independent upper limit showing superiority of slow or fast electrons at small or large separations. (c) Strongly enhanced Smith-Purcell radiation near a BIC. (d) Experimental setup. OBJ, objective (NA = 0.3); BS, beam splitter; SP, spectrometer; CAM, camera. (e-f) SEM images of the structure in (e) top view and (f) cross-sectional view. (g) Quantitative measurement of Smith-Purcell radiation (inset: camera image of the radiation). Solid lines mark the theoretical radiation wavelengths at the normal angle. The envelope (peak outline) of the measured spectra (dots) resemble and trail the theoretical upper limit (shaded to account for fabrication tolerance).

surprisingly, at subwavelength separations *nonrelativistic* electrons offer maximal radiation. Moreover, we reveal that high-quality-factor (high- $Q$ ) resonances near a photonic bound state in the continuum (BIC) enhance Smith–Purcell radiation by orders of magnitude, mirroring a divergence of the upper limit for lossless dielectric media.

We first show our shape-independent upper limit of free electron radiation and energy loss:

$$\Gamma_{\tau}(\omega) \leq \frac{\alpha \xi_{\tau}}{2\pi c} \frac{|\chi|^2}{\text{Im } \chi} \frac{L\psi}{\beta^2} [(\kappa_{\rho}d)K_0(\kappa_{\rho}d)K_1(\kappa_{\rho}d)], \quad (2a)$$

$$\propto \frac{1}{\beta^2} \begin{cases} \ln(1/\kappa_{\rho}d) & \text{for } \kappa_{\rho}d \ll 1, \\ \pi e^{-2\kappa_{\rho}d}/2 & \text{for } \kappa_{\rho}d \gg 1. \end{cases} \quad (2b)$$

These limits are completely general; they set the maximum photon emission and energy loss of an electron beam coupled to an arbitrary photonic environment [Fig. 2(a)] in either the nonretarded or retarded regimes, given only the beam properties and material composition. The key factors that determine maximal radiation are identified: intrinsic material loss (represented by  $\text{Im } \chi$ ), electron velocity  $\beta$ , and impact parameter  $\kappa_{\rho}d$ .

A surprising feature of the limits in Eq. (2) is their prediction for optimal electron velocities. As shown in Fig. 2(b), when electrons are in the far field of the structure ( $\kappa_{\rho}d \gg 1$ ), stronger photon emission and energy loss are achieved by faster electrons—a well-known result. On the contrary, if electrons are in the near field ( $\kappa_{\rho}d \ll 1$ ), *slower* electrons are optimal. This contrasting behavior is evident in the asymptotics of Eq. (2b), where the  $1/\beta^2$  or  $e^{-2\kappa_{\rho}d}$  dependence is dominant at short or large separations.

There is an ostensible peculiarity in the limits: Eq. (1) diverges for lossless materials ( $\text{Im } \chi \rightarrow 0$ ). We find that such divergence points to BICs, an actual physical possibility of enhancing free electron radiation by orders of magnitude [Fig. 2(c)], when specific frequency, phase, and polarization matching conditions are met.

We perform quantitative measurement of Smith–Purcell radiation<sup>4</sup> to directly probe the upper limit. Fig. 2(d) shows our experimental setup. A one-dimensional 50%-filling-factor grating (Au-covered single-crystalline Si)—the quintessential Smith–Purcell setup—is chosen as a sample, and shown by SEM images in Figs. 2(e–f).

Fig. 2(g) depicts our measurements of first order  $m = 1$  Smith–Purcell radiation appearing at wavelengths between 500 and 750 nm. In quantitative agreement with the Smith–Purcell equation<sup>4</sup> at normal emission angle (solid lines), the measured radiation spectra (dots) blueshift with increasing electron velocity. More importantly, we experimentally obtain the absolute intensity of the collected radiation via a calibration measurement, enabling comparisons with the upper limits. The upper limits for the surface-normal emission wavelengths ( $\lambda = a/\beta$ ) are evaluated at the center of the interaction region [height  $\approx 140$  nm ( $kd \approx 1.5$ ), varying with beam energy], and is shown with shading in Fig. 2(g) to account for the thickness uncertainty ( $\pm 1.5$  nm). The envelope (close normal-angle radiation) of the measurements follows the limit lineshape across the visible spectrum: both the theoretical limit and the measured intensities peak near 550 nm and decrease in a commensurate manner for other wavelengths.

#### 4. SYNTHETIC SCATTERING: OBSERVATION OF THE NON-ABELIAN AHARONOV–BOHM EFFECT

In the previous chapters, we investigate the scattering of electromagnetic waves with *real* structures. In this chapter, we will go beyond this scope and discuss the scattering of electromagnetic waves with *synthetic* gauge fields, and consequently, synthetic magnetic fields.

In the original Aharonov–Bohm effect, a particle experience an Abelian (commutative) gauge potential, which imprints a scalar, observable geometric phase in its wave function. In the non-Abelian (non-commutative) generalization of the Aharonov–Bohm effect, the homogeneous Abelian gauge potentials should be replaced with inhomogeneous non-Abelian gauge potentials, which have been theoretically shown to play a pivotal role in the realizations of topological phases and quantum simulations. However, to date, the non-Abelian Aharonov–Bohm effect<sup>5,6</sup> has not been experimentally observed, due to a lack of approaches to both synthesize and also to detect non-Abelian gauge fields in real space.

We report<sup>7</sup> an experimental synthesis of non-Abelian gauge fields in real space and the observation of the non-Abelian Aharonov–Bohm effect with classical waves and classical fluxes. Based on optical mode degeneracy, we break time-reversal symmetry in different manners—via temporal modulation and the Faraday effect—to synthesize tunable non-Abelian gauge fields. We identify the horizontal and vertical transverse modes (denoted by  $|h\rangle$  and  $|v\rangle$  respectively) in optical fibers as the internal pseudospin degree of freedom. Crucially, we synthesize two types of gauge fields,  $\phi\sigma_z$  and  $\theta\sigma_y$ , using two distinct methods to break the time-reversal symmetry.

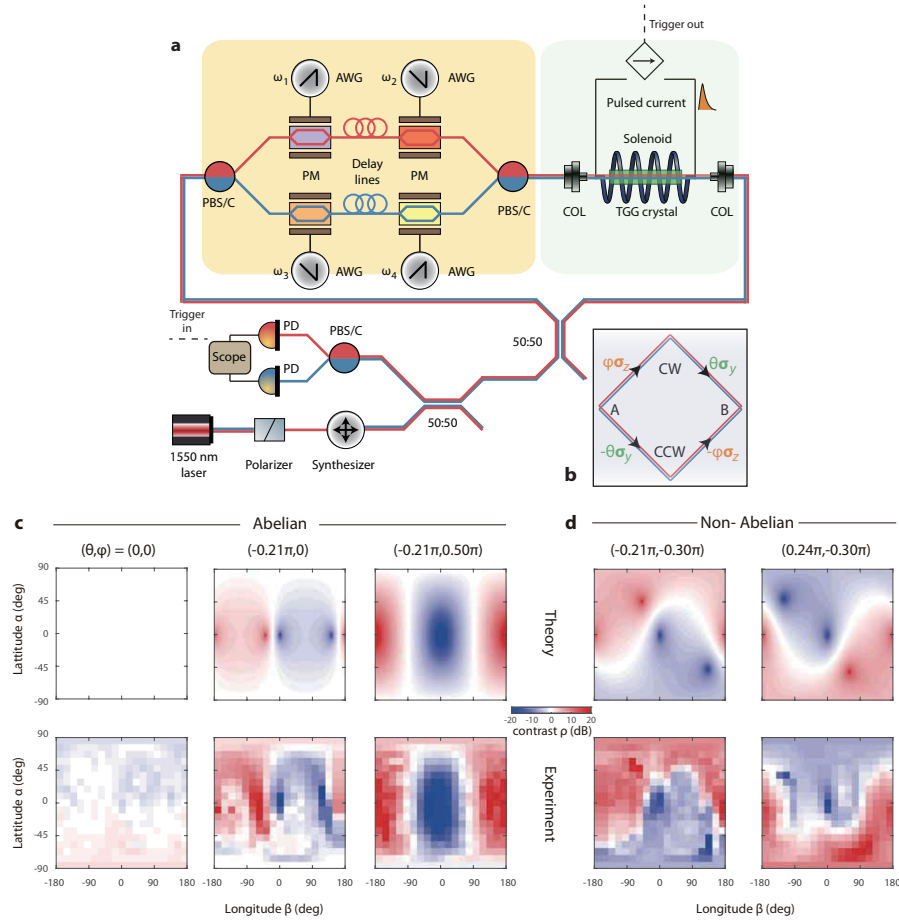


**Figure 3. Non-Abelian Aharonov–Bohm interference.**<sup>7</sup> **a.** Experimental setup. The interference between different final pseudospin states—originated from reversed ordering of the gauge structures [CW and CCW, **(b)**—is read out via a Sagnac interferometer, which gives rise to the non-Abelian Aharonov–Bohm effect. PBS/C: polarization beam splitter/combiner; PM: phase modulator; AWG: arbitrary waveform generator; COL: collimator; TGG: Terbium Gallium Garnet; PD: photodetector. **c-d.** Predicted and observed contrast functions  $\rho$  for Abelian **(c)** and non-Abelian **(d)** gauge fields.

To construct a gauge field of  $\phi\sigma_z$ , we first use dynamic modulations that dress  $|h\rangle$  and  $|v\rangle$  with nonreciprocal phase shifts of  $\pm\phi$ , respectively. Specifically, four LiNbO<sub>3</sub> phase modulators—two (labeled 1 and 2) for  $|h\rangle$  and two (labeled 3 and 4) for  $|v\rangle$ —are driven by arbitrary waveform generators that create phase shifts in the form of sawtooth functions in time (Fig. 3a). Besides dynamic phases,  $|h\rangle$  ( $|v\rangle$ ) picks up an extra phase  $\phi = \omega\tau$  ( $-\omega\tau$ ) in the forward (i.e. left-to-right) direction, but an opposite phase  $-\phi$  ( $+\phi$ ) in the backward direction. This pair of opposite nonreciprocal phases for opposite pseudospin components ( $|h\rangle$  and  $|v\rangle$ ) correspond to a  $\phi\sigma_z$  gauge field, which is continuously tunable by varying the modulation frequency  $\omega$ .

A second, orthogonal type of gauge field,  $\theta\sigma_y$ , is created using the Faraday effect (Fig. 3a). Specifically, light is coupled out of the fiber, sent through a Terbium Gallium Garnet crystal placed in an external magnetic field, and then coupled back into the fiber. Through the Faraday effect, pseudospin of light is rotated in a nonreciprocal



way, which corresponds to a gauge field of  $\theta\sigma_y$ . This gauge field is also continuously tunable through the external magnetic field.

We then concatenate the two non-Abelian gauge fields to demonstrate the non-Abelian Aharonov–Bohm effect via Sagnac interferometry (Fig. 3a and b). Evolved from the clockwise (CW) and counter-clockwise (CCW) paths of the Sagnac loop, the two final states are  $\mathbf{s}_f^{\theta\phi} = \sigma_z e^{i\theta\sigma_y} e^{i\phi\sigma_z} \mathbf{s}_i$  and  $\mathbf{s}_f^{\phi\theta} = e^{-i\phi\sigma_z} e^{-i\theta\sigma_y} \sigma_z \mathbf{s}_i$ , where the  $\sigma_z$  term maintains a consistent handedness of the polarization for counter-propagating states. The interference of the two final states is given by<sup>6</sup>

$$\mathbf{s}_f = \mathbf{s}_f^{\theta\phi} + \mathbf{s}_f^{\phi\theta} = -\sigma_x \left( e^{i\theta'\sigma_y} e^{i\phi\sigma_z} + e^{i\phi\sigma_z} e^{i\theta'\sigma_y} \right) \mathbf{s}_i, \quad (3)$$

where  $\theta' = \theta + \pi/2$  and  $\sigma_x$  is a global spin flip. This interference describes a Sagnac-type realization of the non-Abelian Aharonov–Bohm effect<sup>6</sup>—the interference between two final states, which originate from the same initial state, but undergo reversely-ordered, inhomogeneous path integrals in the CW and CCW directions.

In our experiment, we place a polarization synthesizer in front of the Sagnac loop, to prepare any desired pseudospin state as the input in a deterministic manner, which allows an arbitrary sampling of the Hilbert space. After exiting the Sagnac loop, the two final states  $\mathbf{s}_f^{\theta\phi}$  and  $\mathbf{s}_f^{\phi\theta}$  interfere with each other. The associated interference intensity is projected onto the horizontal and vertical bases, which are then measured separately as  $I_h$  and  $I_v$ . Their contrast  $\rho \equiv I_h/I_v$  between the two intensities are defined as our experimental observable.

We characterize our synthetic gauge fields by measuring the contrast function  $\rho$  (Fig. 3c and d). A comparison is made between theoretical predictions (top row) and experimental measurements (bottom row) for five sampling points on the synthetic space  $T^2$ . We theoretically derive that the necessary and sufficient condition for the gauge fields to become non-Abelian is satisfied when  $\theta \neq m\pi/2$  and  $\phi \neq n\pi/2$ ; the same condition also guarantees the existence of a zero and a pole of the contrast function away from the equator. This criteria is confirmed in our measurements via its direct indication—an off-equator pole/zero, as evident from the comparison between the Abelian (Fig. 3c) and the non-Abelian (Fig. 3d) cases.

## ACKNOWLEDGMENTS

We thank our coauthors Akshay Agarwal, Karl K. Berggren, Hrvoje Buljan, Thomas Christensen, John D. Joannopoulos, Steven G. Johnson, Ido Kaminer, Steven E. Kooi, Philippe Lalanne, Aviram Massuda, Owen D. Miller, Chao Peng, Charles Roques-Carmes, Wei Yan, Bo Zhen, Mengjie Zheng, and Di Zhu for their contributions in the presented works Ref.<sup>1,3,7</sup>

## REFERENCES

- [1] Yang, Y., Zhu, D., Yan, W., Agarwal, A., Zheng, M., Joannopoulos, J. D., Lalanne, P., Christensen, T., Berggren, K. K., and Soljačić, M., “A general theoretical and experimental framework for nanoscale electromagnetism,” *Nature* **576**, 248–252 (2019).
- [2] Feibelman, P. J., “Surface electromagnetic fields,” *Prog. Surf. Sci.* **12**(4), 287–407 (1982).
- [3] Yang, Y., Massuda, A., Roques-Carmes, C., Kooi, S. E., Christensen, T., Johnson, S. G., Joannopoulos, J. D., Miller, O. D., Kaminer, I., and Soljačić, M., “Maximal spontaneous photon emission and energy loss from free electrons,” *Nature Physics* **14**(9), 894 (2018).
- [4] Smith, S. J. and Purcell, E., “Visible light from localized surface charges moving across a grating,” *Physical Review* **92**(4), 1069 (1953).
- [5] Wu, T. T. and Yang, C. N., “Concept of nonintegrable phase factors and global formulation of gauge fields,” *Phys. Rev. D* **12**(12), 3845 (1975).
- [6] Dalibard, J., Gerbier, F., Juzeliūnas, G., and Öhberg, P., “Colloquium: Artificial gauge potentials for neutral atoms,” *Rev. Mod. Phys.* **83**(4), 1523 (2011).
- [7] Yang, Y., Peng, C., Zhu, D., Buljan, H., Joannopoulos, J. D., Zhen, B., and Soljačić, M., “Synthesis and observation of non-abelian gauge fields in real space,” *Science* **365**(6457), 1021–1025 (2019).